

Structural determination and electronic properties of 4d perovskite SrPdO₃

Jiangang He^{1,2} and Cesare Franchini¹

¹University of Vienna, Faculty of Physics and Center for Computational Materials Science, Vienna, Austria

²School of Applied & Engineering Physics, Cornell University, Ithaca, NY 14853, USA

(Dated: July 23, 2018)

The structure and ground state electronic structure of the recently synthesized SrPdO₃ perovskite [A. Galal *et al.*, J. Power Sources, **195**, 3806 (2010)] have been studied by means of screened hybrid functional and the GW approximation with the inclusion of electron-hole interaction within the test-charge/test-charge scheme. By conducting a structural search based on lattice dynamics and group theoretical method we identify the orthorhombic phase with $Pnma$ space group as the most stable crystal structure. The phase transition from the ideal cubic perovskite structure to the $Pnma$ one is explained in terms of the simultaneous stabilization of the antiferrodistortive phonon modes R_4^+ and M_3^+ . Our results indicate that SrPdO₃ exhibits an insulating ground state, substantiated by a GW₀ gap of about 1.1 eV. Spin polarized calculations suggests that SrPdO₃ adopts a low spin state ($t_{2g}^{\uparrow\downarrow\uparrow\downarrow}e_g^0$), and is expected to exhibit spin excitations and spin state crossovers at finite temperature, analogous to the case of 3d isoelectronic LaCoO₃. This would provide a new playground for the study of spin state transitions in 4d oxides and new opportunity to design multifunctional materials based on 4d $Pnma$ building block.

PACS numbers: 61.50.Ah, 71.15.Mb, 71.20.-b, 63.20.-e, 75.10.-b,

I. INTRODUCTION

Owing to the wide range of physical and chemical properties, transition metal (TM) oxides perovskites (chemical formula ABO_3) exhibit a large variety of functional behaviors (Ref.1) and find applications in many technologically relevant fields including superconductivity,^{2,3} multiferroicity,⁴⁻⁶ solid oxide fuel cells,^{7,8} catalysis,⁹ and thermoelectricity.¹⁰ In the last decade, 4d TM perovskites have attracted increasing attention motivated by the numerous intriguing (and to some extent unexpected) properties originating from the delicate balance between the larger spatial extension of the 4d manifold, the reduced Coulomb repulsion and exchange energy, and the increased tendency towards O-2p/TM-4d hybridization.¹¹ As compared to the most widely studied 3d TM oxides, 4d TM perovskites offer a novel physical arena to study the interactions among spin, orbital, electron, and lattice degrees of freedom. Prime examples of these anomalous behaviors (non-Fermi liquid, ferromagnetism, half-metallicity, high-temperature antiferromagnetism, high conductivity, etc.) were recognized in ruthanates,¹²⁻¹⁴ molybdates¹⁵ and technetates.¹⁶⁻¹⁹ In addition to these fundamental issues, the growing concerns about global warming have boosted an intense research on energy production processes based on perovskites. In particular, noble metal incorporated perovskites represent a valuable alternative as catalysts since they have a high thermal stability and their elevated compositional flexibility along with the presence of chemically active structural defects and localized electronic states offer tremendous tailoring possibilities for designing more efficient catalytic processes.^{8,20,21} Palladium oxides is one of the most useful catalyst in oxidation reaction^{22,23} and the incorporation of Pd in perovskite structure turned out to efficiently suppress the inconvenient clustering of

Pd particles, thereby improving the catalytic activity.²⁰

Very recently, SrPdO₃ perovskite with a high catalytic activity toward hydrogen evolution reaction was successfully synthesized for the first time by Galal *et al.* by a citrate method.²⁴ These authors have also shown, that the Curie-Weiss plot derived from the evolution of the molar magnetic susceptibility as a function of temperatures (for temperatures higher than 280 K), exhibits an antiferromagnetic (AFM) character, with a magnetic ordering temperature of about 370 K and a surprisingly large calculated magnetic moment of 5.7 μ_B , suggestive of a high-spin (HS) configuration ($t_{2g}^{\uparrow\uparrow\uparrow}e_g^{\uparrow\uparrow}$) of the Pd⁴⁺ ion.²⁴ Considering that the spin-state of d⁶ perovskites such as LaCoO₃ represents a great challenge for both theory and experiment and have been the source of much controversy^{25,26} these findings should be taken with a certain caution. At low temperature, in fact, LaCoO₃ (isoelectronic to SrPdO₃) poses a low-spin (LS) configuration ($t_{2g}^{\uparrow\downarrow\uparrow\downarrow}e_g^0$) and a diamagnetic semiconducting character.^{27,28} As the temperature is elevated LaCoO₃ exhibits an intricate magnetic phase diagram characterized by an intermediated LS-HS state, possibly associated with a LS-HS crossover,²⁹ whose detailed nature remains highly debated.³⁰ The HS state is usually favored when the crystal field splitting energy is smaller than the Coulomb repulsive energy among electrons. As 4d ions generally have larger crystal field splitting energy and smaller Coulomb repulsive energy than 3d ions, it is expected that 4d TM oxides such as SrPdO₃ would prefer a LS configuration, subjected to spin-state crossover driven by thermal excitations.

The electronic structure and the detailed structural properties of SrPdO₃ remain up to date to be determined. The scope of the present work is to address these issues by means of an accurate *ab initio* analysis performed in the framework of hybrid density function theory and GW ap-

proximation. In particular, we have determined the most favorable crystal symmetry and structural distortions on the basis of a careful analysis of the phonon instabilities starting from the ideal cubic perovskite structure.^{31,32} After describing the computational set-up (Sec. II), we will discuss the results of our structural search (Secs. III A and III B). The electronic properties of the most stable structure will be presented in Sec. III C. The most important outcomes of our study are summarized in the last section.

II. COMPUTATIONAL METHOD

All calculations were performed with the Vienna *ab initio* Simulation Package (VASP).^{33,34} The electron and ion interaction was described within the projector augmented wave (PAW) method.^{35,36} The plane wave basis set cutoff energy was set to 400 eV and the k -space integration was done by adopting a $8 \times 8 \times 8$ Monkhorst-Pack grid for the cubic $P_{m\bar{3}m}$ structure and the same density was kept for all other considered phases. All structures were fully relaxed (including unit cell shape, volume, and internal atomic positions) by using the screened hybrid density functional scheme of Heyd-Scuseria-Ernzerhof (HSE06, Ref.37) until the Hellmann-Feynman forces acting on each atom were smaller than 0.01 eV/\AA .

The phonon dispersion of ideal cubic and ground state P_{nma} perovskite structures were calculated by means of the finite difference method as implemented in PHONOPY,^{38,39} by adopting a $2 \times 2 \times 2$ supercell for both the $P_{m\bar{3}m}$ and P_{nma} phase. The cubic phonon dispersion was computed at HSE06 level, whereas for the larger P_{nma} supercell due to the exceedingly high computational cost we used the Perdew-Becke-Ernzerhof (PBE, Ref. 40) functional and the results were cross-checked by LDA (Ref. 41) and PBEsol (Ref. 42) functionals.

The ground state electronic structure of P_{nma} structure was studied by using HSE with different values of the Hartree-Fock exchange mixing parameter α and the GW approximation (Ref. 43) within the plasmon-pole model as implemented in the VASP code.^{44,45} The GW calculations were performed partially self-consistently, by keeping the screened Coulomb interaction W fixed to the initial W_0 value and iterating only the Green function G until the quasi-particle energies were converged (this was achieved after four iterations). This partial self-consistent procedure is usually referred to as GW_0 . Since the results of GW_0 calculations critically depends on the initial orbitals used to construct the screening properties and on the treatment of excitonic effects,⁴⁶⁻⁴⁸ we have tested both PBE and HSE starting orbitals and for selected cases we have incorporated electrostatic interactions between electrons and hole within the test-charge/test-charge (TC-TC) scheme.⁴⁹ In the GW calculations we have included 320 bands, and the TCTC screening was computed for 80 bands around the Fermi energy.

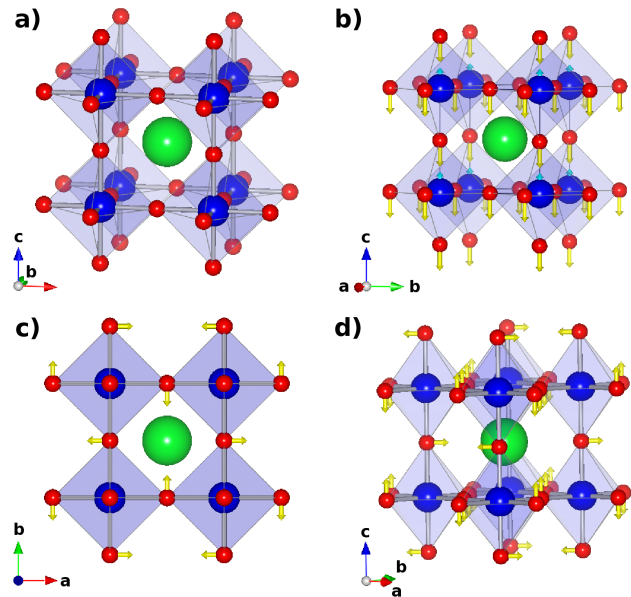


FIG. 1. (Color online) Structural model and relevant phonon displacements. (a) Structure of ideal cubic ($P_{m\bar{3}m}$) SrPdO₃. In (b), (c), and (d) it is shown an illustration of the atomic displacements associated with the symmetry modes Γ_4^- , M_3^+ , and R_4^+ , respectively. Large (green), medium-size (blue) and small (red) spheres indicate Sr, Pd, and O atoms, respectively. The arrows represent the displacement of oxygen and Pd atom.

As already discussed in the introduction the determination of the spin state of d^6 perovskites is affected by large confusion due to the approximation involved in *ab initio* schemes and by the difficulty in reliably extracting the spin state from experimental data. We have scrutinized different magnetic ordering (AFM-A, AFM-C, AFM-G and ferromagnetic, see Ref. 50) and, in line with the results obtained by HSE for LaCoO₃,⁵⁰ we found that all structures are predicted to adopt a LS configuration.

III. RESULTS AND DISCUSSION

In the first part of this section we determine the unstable phonon modes of the high symmetry ($P_{m\bar{3}m}$, No. 221) cubic perovskite structure, which will serve as guidelines to setup the strategy for the structural search. This section ends with the discussion of the ground state electronic properties of the most stable phase of SrPbO₃.

A. Phonon dispersion of cubic phase

The ideal ABO_3 perovskite has cubic symmetry (space group $P_{m\bar{3}m}$, No. 221), and can be structurally interpreted as a framework of corner-sharing BO_6 octahedra with the A cations located at the 12-fold-coordinated

intra-octahedra voids. The stability and distortion of perovskite crystal structures are often discussed in terms of the Goldschmidt's tolerance factor t , $t = (r_A + r_O)/\sqrt{2}(r_B + r_O)$, where r_A , r_B , and r_O are the ionic radii of A, B, and O ions, respectively.^{51,52} $t \approx 1$ represents the ideal conditions upon which the perovskite structure assumes its ideal cubic symmetry. Depending on whether the tolerance factor t is greater or less than 1.0, different kind of distorted structural variants are formed: hexagonal (face-sharing BO_6 octahedra) for $t > 1$, whereas for $t < 0.9$ cooperative rotations of the octahedra yield lower symmetry variants such as tetragonal, orthorhombic, rhombohedral etc.⁵¹ As $SrPdO_3$ has $t = 0.905$ it is expected that the cubic structure is dynamical unstable at low temperature, which could be stabilized throughout suitable rotations and tilting of the octahedra network.

In cubic perovskite, the only free structural parameter is the lattice constant a . The relaxed lattice constant a is predicted to be 3.946 Å at HSE06 level. Spin-polarized calculations shown that the cubic phase of $SrPdO_3$ is a non-magnetic metal, in which the Pd^{4+} cation adopts the LS configuration ($d^{\uparrow\downarrow\uparrow\downarrow}$). Based on the relaxed structure, the HSE06 calculated phonon dispersion curve along the high-symmetry directions Γ -X-M-R- Γ -M is shown in Fig.2. As expected from the above considerations on the tolerance factor, there are many unstable (negative phonon frequency) phonon branches, indicating that the cubic phase of $SrPdO_3$ is dynamically unstable at low temperature. The unstable modes are predominantly associated with O atoms displacement (dashed thick (red) line in Fig.2): The most negative mode at the zone center is the ferroelectric (FE) instability Γ_4^- (we use A site center setting in this paper), which represents the opposite displacement of Pd ion and O octahedra as indicated by the arrows in Fig.1b, whereas at M and R the phonon instabilities are associated with the rotation and tilting of oxygen octahedra (antiferrodistortive, AFD) M_3^+ and R_4^+ , respectively (schematically shown in Fig.1 c and d).⁵³ These instabilities are very common in cubic perovskites and were very well studied.⁵⁴⁻⁵⁶ Having established the phonon instabilities of the ideal cubic phase we now present the outcomes of our structural search, which is based on the stabilization of the negative phonon modes through suitable atomic displacements.

B. Structural search and determination of the most stable phase

From the phonon analysis of the cubic phase, it was concluded that there are three important unstable modes: Γ_4^- , M_3^+ , and R_4^+ . In order to stabilize these unstable modes, we have displaced the atoms according to the force constant eigenvectors and created a pool of subgroup structures. Each of the obtained subgroup structure was then subjected to a full structural relaxation (unit cell shape, volume, and atom positions) within the

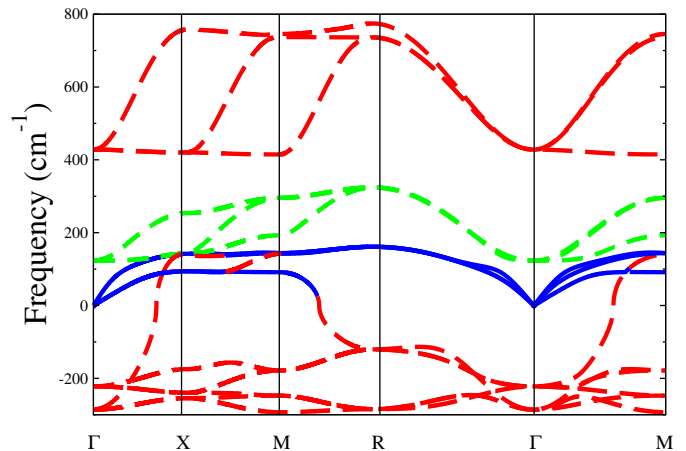


FIG. 2. (Color online) The phonon dispersion curve of $SrPdO_3$ with cubic ($P_{m\bar{3}m}$) space group at level of HSE06. The dark full (blue), light-gray dashed (green) and dark-gray dashed (red) lines indicate a predominantly Sr, Pd, and O character of the dynamic matrix eigenvectors associated with the phonon curves, respectively. The negative phonon branches are mostly associated with O instabilities.

specific subgroup symmetry, i.e. during the relaxation procedure the subgroup symmetry was kept fixed. The comparison of the total energies of the fully relaxed subgroup structures will identify the most stable structural variant.

Clearly, the stabilization of negative phonon modes by moving the atomic positions breaks the cubic symmetry and leads to lower symmetry structures. The total distortion amplitudes of the fully relaxed subgroup structures with respect to cubic phase (reference phase) were calculated by using the Bilbao Crystallographic Server,⁵⁷ and the direction of the order parameter (which is identified by the space group symmetries of the parent and subgroup structure in a phase transition) is obtained according to the group theoretical methods collected in the ISOTROPY Software Suite.⁵⁸ The results are collected in Tab. I where, for each subgroup structure, we summarize the following information: (i) the number of formula units (f.u.) per primitive cell (Z), (ii) the characteristic mode, (iii) the direction of the order parameter (Dir), (iv) the total distortion amplitude (Amp), and finally (v) the total energy of the fully relaxed subgroup structure with respect to the ideal cubic phase (ΔE). The various structural variants included in Tab. I are grouped according to the distinctive unstable modes. Beside including the main unstable modes Γ_4^- , M_3^+ , and R_4^+ , we have also considered the other zone boundary unstable mode, i.e. X (X_5^+), a few second largest instabilities at high symmetry points Γ (Γ_5^-), R (R_5^+), and M (M_5^+), as well as suitable combinations of these modes as detailed below.

Condensing the largest unstable polar mode Γ_4^- in different directions leads to five polar subgroup structures: P_{4mm} , A_{mm2} , R_{3m} , P_m , and C_m , each characterized by

TABLE I. Collection of the relative energies (ΔE , meV/f.u.), unstable modes (Modes), number of formula unit (f.u.) per primitive cell (Z), direction of order parameter (Dir), total distortion amplitude (Amp , Å) of all subgroup structures considered in the structural search and obtained by stabilizing the unstable modes of cubic SrPdO₃.

Subgroup	Z	Modes	Dir	Amp	ΔE
P_{4mm} (99)	1	Γ_4^-	(a,0,0)	0.2570	-136
A_{mm2} (38)	1	Γ_4^-	(a,a,0)	0.2736	-150
R_{3m} (160)	1	Γ_4^-	(a,a,a)	0.2608	-150
P_m (6)	1	Γ_4^-	(a,b,0)	0.2637	-148
C_m (8)	1	Γ_4^-	(a,a,b)	0.2658	-160
P_{4m2} (115)	1	Γ_5^-	(a,0,0)	0.2950	-64
A_{mm2} (38)	1	Γ_5^-	(a,a,0)	0.4363	-144
R_{32} (155)	1	Γ_5^-	(a,a,a)	0.4088	-133
I_4/mcm (140)	2	R_4^+	(a,0,0)	0.9619	-439
$Imma$ (74)	2	R_4^+	(a,a,0)	0.9834	-522
R_{3c} (167)	2	R_4^+	(a,a,a)	1.0040	-512
$C_{2/m}$ (12)	2	R_4^+	(a,b,0)	0.9890	-523
$C_{2/c}$ (15)	2	R_4^+	(a,a,b)	0.9976	-517
I_4/mmm (139)	2	R_5^+	(a,0,0)	0.1903	-11
P_4/mbm (127)	2	M_3^+	(a,0,0)	0.9551	-405
I_4/mmm (139)	4	M_3^+	(a,a,0)	1.3074	-449
$I_{m\bar{3}}$ (204)	4	M_3^+	(a,a,a)	1.2389	-445
I_{mmm} (71)	4	M_3^+	(a,b,c)	1.2849	-442
P_{nma} (51)	2	M_5^-	(a,0,0,0,0,0)	0.2459	-5
C_{mmm} (65)	2	M_5^-	(a,a,0,0,0,0)	0.0025	-91
R_{3m} (160)	4	M_5^-	(a,0,a,0,a,0)	0.3649	-118
$P_{2/m}$ (10)	2	M_5^-	(a,b,0,0,0,0)	0.0026	-63
C_{mme} (67)	2	M_5^+	(a,a,0,0,0,0)	0.0126	-19
P_{nma} (53)	2	M_5^+	(a,a,0,0,a,-a)	0.0454	-5
C_{mcm} (63)	2	X_5^+	(a,0,0,0,0,0)	0.3643	-53
P_{nma} (51)	2	X_5^+	(a,a,0,0,0,0)	0.3898	-57
I_{ma2} (46)	2	$R_4^+ \oplus \Gamma_4^-$	(a,a,0),(a,0,0)	0.9789, 0.0161	-517
R_{3c} (161)	2	$R_4^+ \oplus \Gamma_4^-$	(a,a,a),(a,a,a)	0.9846, 0.0130	-513
P_{nma} (62)	4	$R_4^+ \oplus M_3^+$	(a,a,0),(a,0,0)	1.1814, 0.9727	-576
C_{mcm} (63)	4	$R_4^+ \oplus M_3^+$	(a,0,0),(a,0,0)	0.9850, 1.0374	-542
P_4/mbm (127)	4	$R_4^+ \oplus M_3^+$	(a,0,0),(a,0,0)	0.6874, 0.7218	-224

a distinctive direction of the order parameter, see Tab. I. Both the energy gain and distortion amplitude of these structures with respect to the reference cubic phase are very similar: $\Delta E \approx 150$ meV/f.u. and $Amp \approx 0.26$ Å. This situation does not change much in terms of total energy stability by considering the stabilization of the non-polar mode at the zone center Γ_5^- , which guides the transition towards three low symmetry structures (P_{4m2} , A_{mm2} , and R_{32}). Much lower energy structures were obtained by condensing the tilting mode R_4^+ and rotation mode M_3^+ . The M_3^+ and R_4^+ derived subgroup structures ($M_3^+ \rightarrow P_4/mbm$, I_4/mmm , $I_{m\bar{3}}$, and I_{mmm} ; $R_4^+ \rightarrow I_4/mcm$, $Imma$, R_{3c} , $C_{2/m}$, and $C_{2/c}$) are strongly dis-

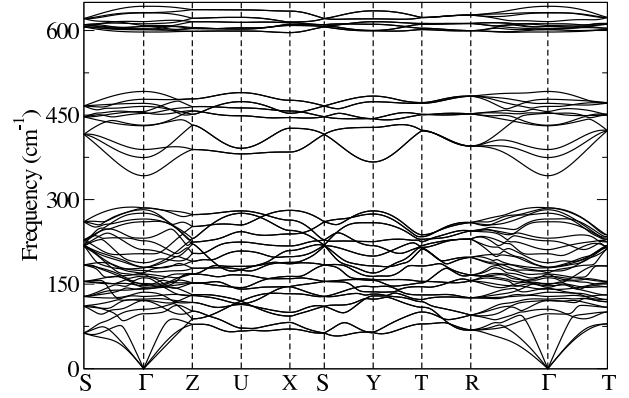


FIG. 3. Phonon dispersion curves of the P_{nma} phase at PBE level.

torted (Amp is in the range 0.95 ~1.31 Å) and show energy gain of about 400 (M_3^+) and 500 (R_4^+) meV/f.u.. It is worth pointing out that the distortion amplitude of the R_4^+ derived structures are not larger than that of M_3^+ , indicating that the stiffness coefficients (defined as $k = (1/2)(\partial^2 E / \partial^2 Q)$, where Q is the amplitude of mode) of the R_4^+ distortion is significantly larger than that of M_3^+ mode. It is obvious that, on the other hand, the stabilization of the second largest unstable phonon modes R_5^+ , M_5^+ , and X_5^+ leads to much less favorable structures.

The fact that the amount of energy gained by condensing the single unstable modes M_3^+ and R_4^+ are much larger than that of Γ_4^- and of the other unstable modes indicates that in SrPdO₃ AFD instabilities are much stronger than FE ones. Therefore AFD instabilities should be considered as primary order parameters, which is similar with other 4d transition metal oxides such as NaNbO₃ and SrZrO₃.^{54,56} Thus, in order to find possibly more stable structures we have considered the combination of R_4^+ and M_3^+ distortions at the same time. Three possible combinations of AFD with different order parameter directions were studied, as shown in Table I: P_{nma} , P_4/mbm , and C_{mcm} . We found, that the most stable structure is P_{nma} (No. 62), which is the combination of R_4^+ in (a,a,0) direction and M_3^+ in (a,0,0) direction, and characterized by a energy gain of 576 meV/f.u..⁵³ The amplitudes of R_4^+ and M_3^+ modes are almost identical to the corresponding single-mode frozen cases indicating that these two modes are compatible with each other at the lower symmetry phase P_{nma} . Moreover, it is found that the energy gain of the combined $R_4^+ \oplus M_3^+$ distortion is larger than the corresponding single-mode frozen cases (R_4^+ and M_3^+).

In order to check the dynamical stability of the P_{nma} phase, we have calculated its phonon dispersion at PBE level (cross-checked by LDA and PBEsol) and did not

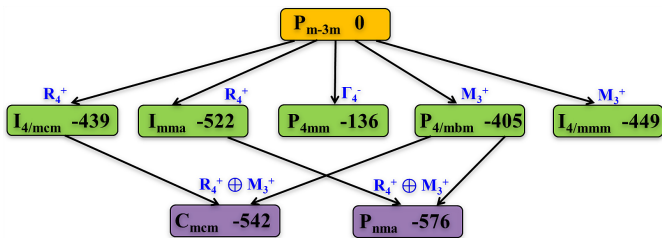


FIG. 4. (Color online) Group and subgroup tree of high symmetry structure ($P_{m\bar{3}m}$) and low-lying structures (P_{nma} and C_{mcm}). The energy gain (meV/f.u.), by condensing unstable modes (blue color), with respect to cubic phase is also indicated using black number.

find any unstable mode, as shown in Fig. 3. As a matter of fact, P_{nma} is the most common space group of TM oxide perovskite structures because it takes into account the flexibility of BO_6 oxygen octahedra network throughout collective rotations and tiltings to optimize the coordinate environment of the cation A .^{59,60} Interestingly, another perovskite structure C_{mcm} has the second lowest energy among all subgroup structures. The C_{mcm} space group originates again from a combination of the M_3^+ and R_4^+ modes, but with different order parameter directions. This further confirms that R_4^+ and M_3^+ are the most important unstable factors in the high symmetry phase. Therefore, P_{nma} could be identified as the ground state structure of $SrPdO_3$.

On the basis of these structural analysis, we can exclude the possibility of antiferroelectricity in $SrPdO_3$. Although the antipolar mode X_5^+ is unstable and connects with the polar mode Γ_4^- by an unstable branch, as shown in Fig. 2, the energy gained by condensing X_5^+ ($\Delta E \sim 60$ meV/f.u.) and Γ_4^- ($\Delta E \sim 150$ meV/f.u.) are much smaller than that of AFD ($\Delta E \sim 500$ meV/f.u.). Thus, it is apparent that $SrPdO_3$ does not fully satisfy the criterion of antiferroelectricity as X_5^+ is too weak to compete with the AFD instability.⁶¹

The most important group and subgroup connections associated with the main distortions analyzed in this study are summarized in Fig. 4. Starting from the undistorted cubic structure $P_{m\bar{3}m}$ the stabilization of the single modes R_4^+ , Γ_4^- , and M_3^+ leads to a subset of subgroup structures with different relative energies. The combination of R_4^+ and M_3^+ AFD modes guides the transition towards the two low-lying structures: the P_{nma} phase, ubiquitous in the perovskite family, and the meta-stable structure C_{mcm} , which was observed in $NaNbO_3$ and proposed as intermediate phase of $SrZrO_3$.^{54,62}

The optimized structural parameters of P_{nma} $SrPdO_3$ are tabulated in Table II. Besides the HSE06 data, the results based on PBE and LDA are also shown for comparison. As compared with HSE06, PBE overestimates all lattice constants, especially a , whereas LDA underestimates lattice constants b and c but overestimates a .

We conclude the discussion of the structural search by comparing the structural distortions in $SrPdO_3$ with

TABLE II. The fully relaxed structural parameters (lattice constants a , b , and c , Volume V_0 , and Wyckoff positions) of ground state $SrPdO_3$ (space group P_{nma} , No. 62) as obtained by HSE, PBE, and LDA.

	Wyckoff site	x	y	z
HSE				
a=5.4933 Å	b=7.8124 Å	c=5.5233 Å	$V_0 = 237$	
Sr	4c	0.45925	0.25000	0.49305
Pd	4a	0.00000	0.00000	0.00000
O ₁	4c	0.00464	0.25000	0.07464
O ₂	8d	0.70647	0.03753	0.79362
PBE				
a=5.6992 Å	b=7.9835 Å	c=5.6402 Å	$V_0 = 257$	
Sr	4c	0.45162	0.25000	0.49016
Pd	4a	0.00000	0.00000	0.00000
O ₁	4c	0.01697	0.25000	0.08190
O ₂	8d	0.70456	0.04086	0.7973
LDA				
a=5.5218 Å	b=7.7942 Å	c=5.5067 Å	$V_0 = 237$	
Sr	4c	0.45307	0.25000	0.49072
Pd	4a	0.00000	0.00000	0.00000
O ₁	4c	0.00952	0.25000	0.07982
O ₂	8d	0.70471	0.03983	0.79627

those of other $4d$ perovskites based on TM atoms which precede Pd in the periodic table: $SrTcO_3$, $SrRuO_3$, and $SrRhO_3$. These compounds also crystallize with the orthorhombic P_{nma} space group at low temperature.^{16,63–65} The most important structural data are collected in Tab.III as a function of the occupation of the $4d$ shell going from $SrTcO_3$ (d^3) to $SrPdO_3$ (d^6). For all these $4d$ perovskites the tolerance factor is very similar, ~ 0.9 . Owing to the full occupation of t_{2g} orbitals (low-spin configuration), $SrPdO_3$ has a smaller volume, no Jahn-Teller (JT) distortions ($Q_2=0.004$ and $Q_3=-0.004$) and the largest $GaFeO_3$ -type (GFO) distortions.

C. Ground state electronic structure

As mentioned previously, spin-polarized calculations show that all the structures considered in this paper are non-magnetic (low spin state, $t_{2g}^{\uparrow\uparrow\downarrow\downarrow\downarrow}e_g^0$). In this section we present the electronic properties of the ground state non-magnetic P_{nma} phase of $SrPdO_3$ based on HSE and many-body GW techniques.

At HSE level, using the 'standard' value of the mixing parameter $\alpha=0.25$ we find that P_{nma} $SrPdO_3$ is a direct band gap semiconductor with a band gap of 1.27 eV. The gap is opened between the fully occupied t_{2g} shell (hybridized with the O p states) and the unoccupied e_g manifold laying on the bottom of the conduction band as illustrated in Figs. 5 and 6. The electronic dispersion in Fig.

TABLE III. Structural parameters of SrTcO₃ (HSE data, Ref.17), SrRuO₃ (Experiment, Ref.64), SrRhO₃ (Experiment, Ref.65) and SrPdO₃ (HSE06, this study) within the P_{nma} space group. The Jahn-Teller Q_2 and Q_3 distortions are defined in accordance with the formula given in Ref. 17: $Q_2 = 2(l - s)/\sqrt{2}$ and $Q_3 = 2(2m - l - s)/\sqrt{6}$ where l , s , and m refer to long (l) and short (s) TM-O₂ in-plane distances and medium (m) TM-O₁ vertical ones.

	SrTcO ₃ ^a	SrRuO ₃ ^b	SrRhO ₃ ^c	SrPdO ₃
4d occupation	d^3	d^4	d^5	d^6
TM Ionic radii (pm) ^d	64.5	62.0	60.0	61.5
tolerance factor	0.8921	0.9031	0.9122	0.9054
Volume	242.74	241.52	242.18	237.04
a	5.543	5.530	5.539	5.493
b	7.854	7.845	7.854	7.812
c	5.576	5.567	5.567	5.523
TM-O ₁	1.990	1.981	1.990	1.996
TM-O ₂ ^l	2.015	1.988	2.040	2.001
TM-O ₂ ^s	1.942	1.984	1.970	1.996
Q_2	0.103	0.003	0.050	0.004
Q_3	0.018	-0.008	-0.025	-0.004
TM-O ₁ -TM	168.76	162.79	161.10	156.12
TM-O ₂ -TM	161.57	162.75	156.52	154.06

^aRef.¹⁷ ^bRef.⁶⁴ ^cRef.⁶⁵ ^dRef.⁶⁸

6 looks similar to the one computed for LaCoO₃,^{30,50,66,67} and is characterized by a valence/conduction band region dominated by t_{2g}/e_g orbitals significantly hybridized with O- p states, in agreement with a formal LS state. The major difference is the bandwidth of the bottom of the conduction band which is much larger in SrPdO₃ (4.0 eV) as compared to LaCoO₃ (3 eV), which reflects the more delocalized nature of 4d electrons.¹⁷

In order to clarify the role of the predominant structural distortions discussed in the previous section on the electronic properties we compare in Fig. 5 the density of states (DOS) of the ideal cubic and P_{nma} cases with those corresponding to the structures containing only one single mode (M_3^+ , R_4^+ , and X_5^+) at standard (i.e. $\alpha=0.25$) HSE06 level. The cubic phase turns out to be metallic, with a very wide e_g unoccupied band crossing the Fermi level. The R_4^+ induces a substantial narrowing of the e_g bands which leads to the opening of a rather large band gap of about 0.9 eV. This is mainly due to the cooperative rotation and tilting of the oxygen octahedra (see Fig.1) which significantly reduces the Pd e_g -O $2p$ hybridization. Conversely, both the M_3^+ (in-plane oxygens rotation) and the X_5^+ (Sr anti-polar displacements) modes are not sufficiently effective in weakening the Pd-O hybridization and therefore are unable to open a sizable gap.

We now address the issue of band gap prediction. The value of the band gap at hybrid functional level depends

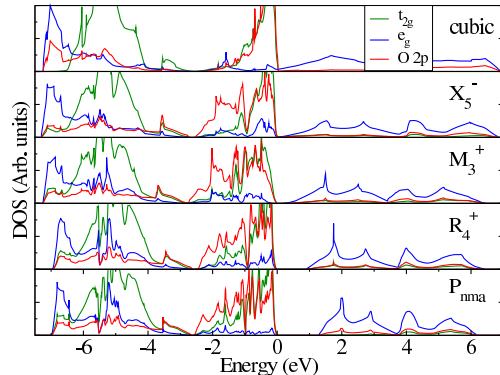


FIG. 5. (Color online) The density of state of SrPdO₃ without distortion (cubic), with distinct M_3^+ , R_4^+ , and X_5^+ distortions, and within P_{nma} symmetry at HSE level for $\alpha = 0.25$.

on the value of the mixing factor α , which determines the amount of exact Hartree-Fock exchange incorporated in the HSE functional. More specifically, there is an almost linear dependence between the band gap and α , as shown for SrPdO₃ in Fig. 7: we found that PBE (equivalent to $\alpha = 0$) is sufficient to open a small gap of 0.24 eV, and by increasing α the gap grows linearly up to 1.27 eV for $\alpha=0.25$ (notice that the choice of α is much less crucial for what concern the structural properties which are well described (i.e. within 1%) for any reasonable value of α). We have discussed this issue in detail in Ref. 50 where we have used a semiempirical rationale for the determination of the optimum mixing factor for HSE in 3d transition metal perovskites which requires the knowledge of the dielectric constant ϵ_∞ .⁶⁹ Unfortunately, the ϵ_∞ of SrPdO₃ is unknown and this hampers a precise estimation of the optimum α for SrPdO₃, as the *ab initio* calculation of the dielectric properties is by far not trivial.^{47,69}

The most accurate way to overtake this limitation is to go beyond generalized Kohn-Sham (gKS) orbitals such as HSE and rely on more sophisticated and computationally much more demanding many-body techniques such as GW.⁴³ The performance and the predictive power of GW-based approaches critically depends on the treatment of the dynamically screened Coulomb potential W and, to a lesser extent, on the self-consistency in G . It has been shown that the results obtained within the widely used single-shot G_0W_0 and partially self-consistent GW_0 approximations depend significantly on the starting point for the solution of the quasiparticle equation.^{46,47} In general, gKS functionals are considered to be good starting points only if electron-hole interactions are incorporated. This is due to the fact that $GW_0@HSE$ within the so called random phase approximation (RPA, i.e. excluding excitonic effects in the calculation of the screened Coulomb interaction) leads to a significant underestimation of the static screening resulting in too large band

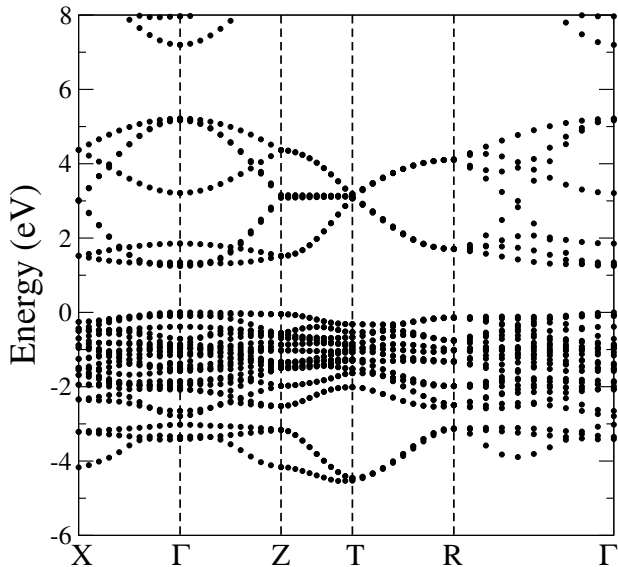


FIG. 6. Band structure P_{nma} -structured SrPdO_3 as computed by HSE for $\alpha = 0.25$.

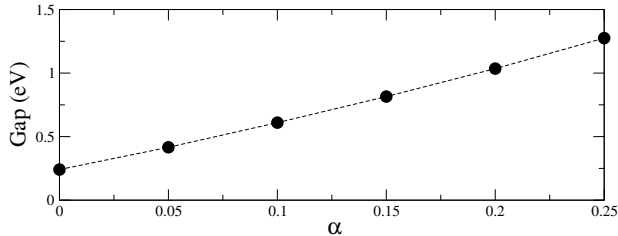


FIG. 7. Dependence of the HSE band gap as a function of the mixing parameter α .

gap.⁴⁷ Conversely, considering that LDA and PBE functionals usually provide reasonable screening properties, the GW_0 @PBE usually deliver band gaps in good agreement with experiment.⁴⁷ Following these arguments here we compare the results obtained from two different procedures: (i) GW_0 @PBE (partially self consistent GW on top of PBE orbitals within the RPA approximation), and (ii) GW_0 -TCTC@HSE (partially self-consistent GW on top of HSE orbitals plus inclusion of excitonic effects via the TCTC kernel⁴⁹). Clearly, the optimum approach would require a self-consistent computation of W , which would render the corresponding GW results free of any dependence on the starting orbitals. Unfortunately, the enormous computational load associated with this scheme prevents its applicability to the present case, mostly due to large size of the unit cell which contains 20 atoms. To date, the only application of fully self-consistent quasi-particle GW plus vertex corrections for non-cubic perovskite is the case of BaBiO_3 , whose unit cell contains *only* 10 atoms.⁴⁸

The results on the band gap are collected in Tab.IV. The application of GW always leads to an increase of the band gap with respect to the corresponding starting

PBE and HSE value (first row of Tab. IV. The converged GW_0 @PBE value is 0.92 eV, whereas the GW_0 -TCTC@HSE estimations ranges between 1.03 eV to 1.31 eV, depending on the value of α . As shown in the last column of Tab. IV the relative deviations among the various schemes are intimately connected with the computed values of the dielectric constant ϵ_∞ , which progressively decreases as a function of α . By averaging over the different starting points our GW_0 data suggest that the band gap of SrPdO_3 is 1.1 ± 0.2 eV.

IV. SUMMARY AND CONCLUSIONS

Summing up, in this study we have performed an accurate structural determination of the novel perovskite SrPdO_3 , based on an appropriate stabilization of the unstable phonon modes found in the ideal perovskite phase by applying symmetry analysis and group theory considerations. We found that the combination of AFD displacements associated with the R_4^+ and M_3^+ modes drives the transition from the unstable cubic phase to the orthorhombic P_{nma} ground state, characterized by a large tilting of the BO_6 oxygen octahedra as reflected by the significant GFO-like distortions. This is in line with the structural properties of the $4d$ perovskite series SrRO_3 , with $R=\text{Tc, Ru, and Rh}$. The ground state electronic structure was studied by using partially self-consistent GW on top of both PBE and HSE orbitals, and including electron-hole interaction in the framework of the TCTC scheme. Our results indicate that low temperature SrPdO_3 is a low-spin state insulator with a band gap of ≈ 1.1 eV. The electronic transition from the metallic ideal cubic phase to the insulating P_{nma} one is mostly driven by the structural distortions associated with the R_4^+ mode which strongly attenuates the O_p - Pd_{e_g} hybridization. The experimentally observed high-temperature antiferromagnetic behavior might originate from spin state excitations, possibly subjected to spin-state crossovers, in similarity with the case of iso-electronic LaCoO_3 . We hope that our study will spur further research aiming to clarify the spin structure of this novel perovskite, for instance by investigating its nuclear hyperfine interaction, to provide an experimental measurement of the band gap in support to our predictions, and, from an application point of view, will help the understanding and optimization of the reported high catalytic activity, and the designing of novel materials with tunable functionalities based on the P_{nma} building block.^{70,71}

V. ACKNOWLEDGMENTS

Research in Vienna was sponsored by the FP7 European Community grant ATHENA. All calculations were performed at the Vienna Scientific Cluster (VSC).

TABLE IV. Band gap of SrPdO₃ calculated by using HSE with different α ($\alpha=0$ refers to PBE calculations), GW₀ and GW₀-TCTC. The value of ϵ_∞ computed within GW₀-TCTC is also shown.

α	0.00	0.05	0.10	0.15	0.20	0.25
HSE(α)	0.24	0.41	0.61	0.81	1.03	1.27
GW ₀ @HSE(α)	0.92	1.08	–	1.31	–	1.43
GW ₀ -TCTC@HSE(α)	–	1.03	–	1.21	–	1.31
ϵ_∞	16.6	13.7	–	10.9	–	9.5

- ¹ I. Vrejoiu, M. Alexe, D. Hesse, and U. Gösele, *Adv. Func. Mater.* **18**, 3892 (2008).
- ² Y. Maeno, H. Hashimoto, K. Yoshida, S. Nishizaki, T. Fujita, J. G. Bednorz, and F. Lichtenberg, *Nature (London)* **372**, 532 (1995).
- ³ H. U. Habermeier, *Mater. Today* **10**, 34 (2007)
- ⁴ T. Kimura, *Annu. Rev. Mater. Res.* **37**, 387 (2007).
- ⁵ R. Ramesh, N. A. Spaldin, *Nat. Mater.* **6**, 21 (2007).
- ⁶ A. Stroppa, P. Barone, P. Jain, J. M. Perez-Mato, S. Piccozzi, *Adv. Mater.* **25** 2284 (2013).
- ⁷ S. B. Adler, *Chem. Rev.* **104**, 4791 (2004).
- ⁸ J. Suntivich, H. A. Gasteiger, N. Yabuuchi, H. Nakanishi, J. B. Goodenough and Y. Shao-Horn, *Nature Chem.* **3** 546 (2011).
- ⁹ M. Misono, *Cat. Today* **100**, 95 (2005).
- ¹⁰ H. Ohta, *Mater. Today* **10**, 44 (2007).
- ¹¹ Y. S. Lee, J. S. Lee, T. W. Noh, D. Y. Byum, K. Soo Yoo, K. Yamaura, and E. Takayama-Muromachi, *Phys. Rev. B* **67**, 113101 (2003).
- ¹² P. B. Allen, H. Berger, O. Chauvet, L. Forro, T. Jarlborg, A. Junod, B. Revaz, and G. Santi, *Phys. Rev. B* **53**, 4393 (1996).
- ¹³ P. Kostic, Y. Okada, N. C. Collins, and Z. Schlesinger, *Phys. Rev. Lett.* **81**, 2498 (1998).
- ¹⁴ J. M. Rondinelli, N. M. Caffrey, S. Sanvito, and N. A. Spaldin *Phys. Rev. B* **78**, 155107 (2008).
- ¹⁵ I. Nagai, N. Shirakawa, S. Ikeda, R. Iwasaki, H. Nishimura, and M. Kosaka, *Appl. Phys. Lett.* **87**, 024105 (2005).
- ¹⁶ E. E. Rodriguez, F. Poineau, A. Llobet, B. J. Kennedy, M. Avdeev, G. J. Thorogood, M. L. Carter, R. Seshadri, D. J. Singh, and A. K. Cheetham, *Phys. Rev. Lett.* **106**, 067201 (2011).
- ¹⁷ C. Franchini, T. Archer, J. He, X. Chen, A. Filippetti, and S. Sanvito, *Phys. Rev. B* **83**, 220402(R) (2011).
- ¹⁸ S. Middey, A. Kumar Nandy, S. K. Pandey, P. Mahadevan, and D. D. Sarma, *Phys. Rev. B* **86**, 104406, (2012).
- ¹⁹ J. Mravlje, M. Aichhorn, and A. Georges, *Phys. Rev. Lett.* **108**, 197202 (2012).
- ²⁰ Y. Nishihata, J. Mizuki, T. Akao, H. Tanaka, M. Uenishi, M. Kimura, T. Okamoto, and N. Hamada, *Nature* **418**, 164 (2002).
- ²¹ C. Sun, R. Hui, and J. Roller, *J. Solid State Electrochem* **14**, 1125 (2010).
- ²² J. A. Yeung, K. Chen, A. T. Bell, and E. Iglesia, *J. Catal.* **188**, 132 (1999).
- ²³ L. Meng, A. P. Jia, J. Q. Lu, L. F. Luo, W. X. Huang, and M. F. Luo, *J. Phys. Chem. C* **115**, 19789 (2011).
- ²⁴ A. Galal, N. F. Atta, S. A. Darwish, A. A. Fatah, S. M. Ali, *J. Power Sources*, **195**, 3806 (2010).
- ²⁵ J.B. Goodenough, *Localized to Itinerant Electronic Transition in Perovskite Oxides*, (Springer, New York, 20011), and references therein.
- ²⁶ C. N. R. Rao, Md. M. Seikh, and C. Narayana, *Top. Curr. Chem* **234**, 1 (2004), and references therein.
- ²⁷ T. Saitoh, T. Mizokawa, A. Fujimori, M. Abbate, Y. Takeda, and M. Takano, *Phys. Rev. B* **55**, 4257 (1997).
- ²⁸ Y. Tokura, Y. Okimoto, S. Yamaguchi, and H. Taniguchi, *Phys. Rev. B* **58**, R1699 (1998).
- ²⁹ P. M. Raccah and J. B. Goodenough, *Phys. Rev.* **155**, 932 (1967).
- ³⁰ H. Hsu, P. Blaha, R. M. Wentzcovitch, and C. Leighton *Phys. Rev. B* **82**, 100406(R) (2010), and references therein.
- ³¹ K. Parlinski and Y. Kawazoe, *Eur. Phys. J. B* **16**, 49 (2000).
- ³² A.I. Lebedev, *Phys. Solid State* **51**, 341 (2009).
- ³³ G. Kresse and J. Hafner, *Phys. Rev. B* **48**, 13115 (1993).
- ³⁴ G. Kresse and J. Furthmüller, *Comput. Mater Sci.* **6**, 15 (1996).
- ³⁵ P. E. Blöchl, *Phys. Rev. B* **50**, 17953 (1994).
- ³⁶ G. Kresse and D. Joubert, *Phys. Rev. B* **59**, 1758 (1999).
- ³⁷ J. Heyd, G. E. Scuseria, and M. Ernzerhof, *J. Chem. Phys.* **118**, 8207 (2003); **124**, 219906 (E) (2006).
- ³⁸ K. Parlinski, Z. Q. Li, and Y. Kawazoe, *Phys. Rev. Lett.* **78**, 4063 (1997).
- ³⁹ A. Togo, F. Oba, and I. Tanaka, *Phys. Rev. B* **78**, 134106 (2008).
- ⁴⁰ John P. Perdew, Kieron Burke, and Matthias Ernzerhof, *Phys. Rev. Lett.* **77**, 3865 ((1996).
- ⁴¹ D. M. Ceperley and B. J. Alder, *Phys. Rev. Lett.* **45**, 566 (1980).
- ⁴² J. P. Perdew, A. Ruzsinszky, G. Csonka, O. A. Vydrov, G. E. Scuseria, L. A. Constantin, X. Zhou and K. Burke, *Phys. Rev. Lett.* **100**, 136406 (2008).
- ⁴³ L. Hedin, *Phys. Rev.* **139**, A796 (1965).
- ⁴⁴ M. Shishkin and G. Kresse, *Phys. Rev. B* **74**, 035101 (2006).
- ⁴⁵ M. Shishkin and G. Kresse, *Phys. Rev. B* **75**, 235102 (2007).
- ⁴⁶ F. Fuchs, J. Furthmüller, F. Bechstedt, M. Shishkin and G. Kresse, *Phys. Rev. B* **76**, 115109 (2007).
- ⁴⁷ Joachim Paier, Martijn Marsman, and Georg Kresse, *Phys. Rev. B* **78**, 121201(R) (2008).
- ⁴⁸ C. Franchini, A. Sanna, M. Marsman, and G. Kresse, *Phys. Rev. B* **81**, 085213 (2010).

- ⁴⁹ F. Bruneval, F. Sottile, V. Olevano, R. Del Sole, and L. Reining, *Phys. Rev. Lett.*, **94**, 186402 (2005).
- ⁵⁰ J. He and C. Franchini, *Phys. Rev. B* **86**, 235117 (2012).
- ⁵¹ V. M. Goldschmidt, *Naturwissenschaften* **14**, 477 (1926).
- ⁵² R. D. Shannon, *Acta Crystallogr., Sect. A* **32**, 751 (1976).
- ⁵³ C. J. Howard and H. T. Stokes, *Acta Crystallogr., Sect. B: Struct. Sci.* **54**, 782 (1998); **58**, 565 (2002).
- ⁵⁴ S. Amisi, E. Bousquet, K. Katcho, and Ph. Ghosez, *Phys. Rev. B* **85**, 064112 (2012).
- ⁵⁵ Ph. Ghosez, E. Cockayne, U. V. Waghmare, and K. M. Rabe, *Phys. Rev. B* **60**, 836 (1999).
- ⁵⁶ R. Machado, M. Sepliarsky, and M. G. Stachiotti, *Phys. Rev. B* **84**, 134107 (2011).
- ⁵⁷ M. I. Aroyo, A. Kirov, C. Capillas, J. M. Perez-Matoj, and H. Wondratschek, *Acta Cryst.* **A62**, 115 (2006); M. I. Aroyo, J. M. Perez-Mato, D. Orobengoa, E. Tasci, G. de la Flor, A. Kirov, *Bulg. Chem. Commun.* **43**(2) 183-197 (2011); M. I. Aroyo, J. M. Perez-Mato, C. Capillas, E. Kroumova, S. Ivantchev, G. Madariaga, A. Kirov & H. Wondratschek, *Z. Krist.* **221**, 1, 15-27 (2006); D. Orobengoa, C. Capillas, M.I. Aroyo, and J. M. Perez-Mato, *J. Appl. Cryst.* **A42**, 820 (2009).
- ⁵⁸ H. T. Stokes, D. M. Hatch, and B. J. Campbell, (2007). ISOTROPY, stokes.byu.edu/isotropy.html.
- ⁵⁹ P. M. Woodward, *Acta Crystallographica* **B53**, 44 (1997).
- ⁶⁰ M. W. Lufaso and P. M. Woodward, *Acta Crystallographica* **B57**, 725 (2001).
- ⁶¹ K. M. Rabe, in *Functional Metal Oxides: New Science and Novel Applications*, ed. by Satish Ogale and V. Venkateshan, Wiley-VCH, Weinheim (2013).
- ⁶² C. N. W. Darlington and K. S. Knight, *Acta Crystallographica* **B55**, 24 (1999).
- ⁶³ S. N. Bushmeleva, V. Yu, Pomjakushin, E. V. Pomjakushina, D. V. Sheptyakov, A. M. Balagurov, *J. Magn. Mater.* **305**, 491 (2006).
- ⁶⁴ C. W. Jones, P. D. Battle, and P. Lightfoot, *Acta Crystallogr., Sect. C: Cryst. Struct. Commun.* **45**, 365 (1989).
- ⁶⁵ K. Yamaura and E. Takayama-Muromachi, *Phys. Rev. B* **64**, 224424 (2001).
- ⁶⁶ Y. Nohara, S. Yamamoto, and T. Fujiwara, *Phys. Rev. B* **79**, 195110 (2009).
- ⁶⁷ K. Knížek, Z. Jiráček, J. Hejtmánek, P. Novák, and W. Ku, *Phys. Rev. B* **79**, 014430 (2009).
- ⁶⁸ R. D. Shannon and C. T. Prewitt, *Acta Crystallogr. Sec. B* **25**, 925 (1969).
- ⁶⁹ A. Alkauskas, P. Broqvist, S. Pasquarello, *Phys. Status solidi (b)* **248**, 775 (2010).
- ⁷⁰ J. M. Rondinelli and C. J. Fennie, *Adv. Mater.* **24**, 1961 (2012).
- ⁷¹ A. T. Mulder, N. A. Benedek, J. M. Rondinelli, and C. J. Fennie, *Adv. Funct. Mater.* **23**, 4810 (2013).